Advanced Powder Technology 30 (2019) 2548–2554

Contents lists available at ScienceDirect

Advanced Powder Technology

journal homepage: www.elsevier.com/locate/apt

Original Research Paper

Ball-milling properties and sintering behavior of Fe-Tm_2O_3 mixture powders

Yongshuai Mu, Guang Ran *, Weisong Wu, Chao Ye

College of Energy, Xiamen University, Xiamen City, Fujian Province 361102, China

ARTICLE INFO

Article history:
Received 1 September 2018
Received in revised form 20 April 2019
Accepted 5 August 2019
Available online 12 August 2019

Keywords:
Iron matrix composites
Neutron absorber
Powder metallurgy
Microstructure
Thulium oxide

ABSTRACT

Aimed at the existing problems of current neutron absorbers that were used in control rods to safely operate a nuclear reactor, new type of Fe-based Tm_2O_3 composites and Fe-based $TmFeO_3$ composites, which were synthesized from the Fe-25.68 wt.%Tm_2O_3 mixture powders by ball milling, cold isostatic pressing and sintering, were designed as next generation neutron absorbers in the present work. During ball milling, Tm_2O_3 was fined, nano-crystallized, amorphized and then dissolved into Fe crystal lattice to form Fe (Tm, O) nanocrystalline solid solution. The effect of sintering temperature and oxygen content at sintering environment on the phases of the sintered bulks were researched, and the corresponding mechanism was discussed. Nanoscale $TmFeO_3$ and Tm_2O_3 particles were distributed in the sintered bulk matrix. The microhardness, compression strength, and the coefficients of thermal expansion of the bulks sintered at different conditions were measured and discussed. The coefficient of linear expansion and compressive strength increased with increasing ball-milling time. The microhardness increased with increasing sintering temperature when the temperature was lower than 1200 °C. Meanwhile, the microhardness and compressive strength of Fe-based Tm_2O_3 composites were larger than that of Fe-based $TmFeO_3$ composites, opposite for the coefficients of thermal expansion.

1. Introduction

Due to the excellent physical and chemical properties, rare earth elements are widely used in nuclear materials, such as nuclear fuels, neutron absorbers, structure materials and etc. Because of the large neutron absorption cross-section, some rare earth elements are used as neutron absorbers in nuclear reactor control rods, such as hafnium (Hf) [1,2], europium (Eu) [3], dysprosium (Dy) [4–6], terbium (Tb) [7,8] and thulium (Tm) [9]. Control rods having neutron absorbers with these rare earth elements are very important in both operating and accident conditions because nuclear reactivity needs to be controlled to safely operate a nuclear reactor. The types of neutron absorbers main include ceramic materials, metal matrix composites and metal alloys. Elemental Hf was first used as the control rod materials in U.S. Naval nuclear reactors and subsequently applied in Indian Point Unit 1 and Yankee Rowe PWR in the 1950s and 1960s [1]. However, it is difficult to separate from zirconium element, elemental Hf is rarely used in neutron absorbers at present. Eu_2O_3 was once used as neutron absorbers in the fast neutron reactor, BOR-60 [3], but in fact, mainly used as neutron poison in nuclear fuels. Dy_2TiO_5 was used as neutron absorber in Russian thermal reactors, such as VVER-1000 RCCAs [6], however, its neutron absorption ability decreases quickly with increasing service time. Therefore, it is important to develop new neutron absorbers with excellent comprehensive performances in the service for a long time, such as stable neutron absorption ability, high irradiation resistance, low coefficient of thermal expansion, high thermal stability and melting point. Based on the outstanding nuclear characteristic of elemental thulium, Fe-based neutron absorbers having thulium atoms will be excellent candidates in control rods.

The sintering parameters, which include sintering atmosphere, temperature, time and etc, obviously affect the microstructure and phase components of the bulks. For example, in the Fe-Al_2O_3 system, Colaianni [10] obtained the phase components containing Fe and Al_2O_3 in the bulks sintered at 900–1200 K with 1×10^{-8} Pa air pressure. However, Sakata [11] synthesized Fe(Fe, Al)$_2O_4$ phase in the bulks sintered at 1450 K with 1×10^{-3} Pa air pressure. Seemingly, the different experiment results are attributed to the vacuum degree. However, the key reason should be oxygen content in the sintering atmosphere. Similar experiment phenomena appeared in the Fe-Y_2O_3 system. When Fe-Y_2O_3 mixture powders were annealed in argon atmosphere [12], Y-Fe-O reacted and the

* Corresponding author.
E-mail address: gran@xmu.edu.cn (G. Ran).

https://doi.org/10.1016/j.apt.2019.08.001

$YFeO_3$ phase was obtained. However, the chemical reaction didn't occur when Fe-Y_2O_3 mixture powders were annealed in hydrogen atmosphere [13]. Katsura [14] found that the formation of Fe-Tm-O compounds depended on the sintering temperature and oxygen partial pressure for studying the thermodynamic properties of Fe-Tm-O compounds at the temperature ranged from 1150 to 1250 °C. Therefore, whether the synthesis of Fe-based Tm_2O_3 or Fe-based $TmFeO_3$ metal matrix composites prepared by the Fe-Tm_2O_3 mixture powders should be determined by the sintering conditions. However, almost no studies relating to the sintering behavior of Fe-Tm_2O_3 mixture powders can be found at present, as well as for the microstructure, mechanical properties, thermophysical properties and physical efficiency of their sintered bulks.

In this work, the ball-milling properties and sintering behavior of Fe-Tm_2O_3 mixture powders were fully investigated, especially for the sintering atmosphere effect on the phase components in the bulks. The microstructures of the ball-milled powders and sintered bulks were observed and discussed. Meanwhile, the effects of preparation parameters on the microhardness, compression strength, and thermal expansion of the sintered bulks were also analyzed.

2. Material design and experiment methods

2.1. Material design

Natural thulium consists of one stable isotope, Tm^{169}. The thermal neutron absorption cross-section of Tm^{169} is 105 barns [15]. Both Tm decay products, Yb and Lu, and their offspring decay products can also absorb neutrons and have similar neutron absorption cross-section. Therefore, in-service, the gray control rod assemblies of loaded neutron absorbers with elemental Tm still have a nuclear reactivity worth that is close to the initial value after a long time of burnup. Even if they are burned up for 20 years, the nuclear reactivity worth is changed only slightly [16]. According to nucleon calculation, nuclear property assessment and burnup analysis, a Φ2.0 mm cylindrical bulk with pure Tm element will be an excellent candidate using as a neutron absorber in gray control rods based on the typical fuel assemblies with 17 × 17 rods used in pressurized water reactor [16,17]. However, the cylindrical bulks with pure Tm are hardly applied to the nuclear reactor core. The reasons should be due to the followings: (1) Because elemental Tm has high chemical relativity and is easily oxidized, and also it is impossible without oxygen in the in-service environment of neutron absorbers. Tm will be oxidized to thulium oxide, which will induce the change of coefficient of thermal expansion, mechanical properties, resistance of neutron radiation and corrosion properties. (2) The 2.0 mm diameter is much smaller than that of inner diameter of gray control rods. In fact, in the AP1000 nuclear power plant, the outer diameter and thickness of the designed gray control rods are usually ranged from 9.4 to 11.43 mm and from 0.254 to 2.54 mm, respectively [17]. Moreover, for the construction and running of AP1000 in China, the outer diameter and thickness of stainless steel pipes is 9.68 mm and 0.47 mm, respectively [8]. (3) From the considerations of manufacturing cost, the price of pure Tm material (over 600 dollar per kilogram, 99.9% purity) is much higher than that of thulium oxide (about 150 dollar per kilogram, 99.99% purity). Therefore, a large-sized bulk with thulium oxide and excellent diluent will be an idea neutron absorber.

Iron has excellent properties of resistance to irradiation damage. The irradiation swelling of annealed Fe was only 1.7% after irradiation to 25.8 dPa (displacement per atom) with a 4×10^{-7} -dPa/s dose in the BR-10 fast reactor [18]. The iron was not obviously affected by transmutation products after exposure with high neutron dose in two fast reactors (BOR-60 and BN-350) at 345–650 °C because much less helium was generated [19]. Meanwhile, Fe component has high melting temperature, high temperature strength, low heat expansion coefficient and excellent thermal conductivity. Importantly, the thermal neutron absorption cross-section of elemental Fe and O is only 2.3 barns and 0.19 barns, respectively [15]. Compared with that of Tm, these values could be neglected, which has little effect on the behavior of nuclear characteristics of bulk materials during long-term burn-up. The main function of Fe and O components is dilution effect and then increases the size of pillars at a certain line density of Tm element in neutron absorber. Therefore, Fe-based metal matrix composites with elemental Tm are considered as potential candidate materials used in gray control rod in nuclear power plant reactor, which can utilize not only the excellent properties of iron component but also the outstanding nucleon characteristics of elemental Tm.

To satisfy the reactivity worth of neutron absorbers in gray control rods, the linear density of elemental Tm in pillars should be kept to 0.6592 g/cm. When the pillars with Φ6.80 mm in diameter are used in PWR, the powder mixtures with Fe-25.68 wt.%Tm_2O_3 are obtained and used to synthesis the bulk neutron absorbers in the present work.

2.2. Experiment methods

The powders of Tm_2O_3 (99.6% purity) and Fe (99.9% purity) with an average particle diameter of 5 μm and 38 μm, respectively, were used as raw materials. Tm_2O_3 powder was purchased from Beijing HWRK Chem Co., LTD. Fe powder was purchased from Changsha Tianjiu Chem Co., LTD. Fe-25.68 wt.%Tm_2O_3 powder mixtures were milled on a SFM-1 high-energy planetary ball mill at room temperature under argon atmosphere. The stainless steel can with 250 mL in volume and the stainless steel balls with 5 mm in diameter were used as milling media. The ball-to-powder mass ratio was 10:1. The rotational speed was 380 rpm. To prevent excessive cold welding and aggregation amongst powder particles, less than 1.5% stearic acid as the process control agent was added in the Fe-25.68 wt.%Tm_2O_3 powder mixtures. The mixtures milled for various time were used to analyze microstructure and phases.

The green bodies were obtained by cold isostatic pressing with 280 MPa hydraulic pressure for 0.5 h from the powder mixtures and then sintered at different temperature for 24 h in a tube furnace with argon protection. To avoid the oxidation during the sintering, the green bodies were previously loaded into a corundum crucible that was sealed using Al_2O_3 adhesion agent in the glove box protected by high pure argon gas (#1 sintering condition). In order to carry out the comparative study, some green bodies without corundum crucible protection were sintered in a tube furnace with argon atmosphere (#2 sintering condition).

The powder mixtures milled for different time were characterized in detail by X-ray diffraction (XRD) on a Rigaku Ultima IV X-ray diffractometer with Cu Kα radiation (λ = 0.1540598 nm), as well as for the sintered bulks. The lattice constant and grain size of Fe phase was obtained by Rietveld refinement method in JADE software. Three main diffraction peaks of Fe were applied to calculate the lattice constant and grain size of Fe phase.

TEM samples of the mixture powders were prepared as follows: the ball-milled mixtures were first put in ethyl alcohol, and then adequately dispersed by ultrasonic vibration. A carbon-coated copper grid was used to collect the dispersed powders in the ethyl alcohol and then dried by ultraviolet lamp. TEM samples of sintered Fe-based composites were prepared by focused ion beam (FIB) on a Hitachi NB5000 instrument. The microstructure of the ball-milled powders and the sintered bulks was examined and analyzed using transmission electron microscopy (TEM) on a JEM-2100 instrument. The microhardness tests of the sintered bulks

were measured on a THVS-1M-AD instrument. The compressive strength tests of the sintered bulks were carried out on a WDW-100E universal testing machine. The coefficient of thermal expansion of the sintered bulks was tested using Netzsch DIL 402C thermal dilatometer.

3. Results and discussions

3.1. Microstructure of the ball-milled powders

Fig. 1 shows the XRD patterns of Fe-25.68 wt.%Tm_2O_3 powder mixtures milled for different time. In the XRD spectrum of the original powder mixtures, there are the diffraction peaks of Fe with body-centered cubic crystal structure and Tm_2O_3 with cubic crystal structure. The diffraction peaks of Tm_2O_3 and Fe are broadened and reduced in intensity with increasing ball-milling time. The broadening of the X-ray diffraction peak is associated with the refinement of grain size, lattice distortion and instrument-induced factor. After 48 h of ball milling, the diffraction peaks of Fe phase still can be observed, indicating that Fe phase keeps crystal structure. However, the weak and broad main diffraction peaks of Tm_2O_3 can be detected, which indicates that Tm_2O_3 is transformed from the crystal to the amorphization. After ball milling for 120 h, only diffraction peaks of Fe phase can be observed, which indicates that Fe phase still keeps a crystal structure. Due to the long-time milling, the peaks of Tm_2O_3 disappear. The diffraction intensity of amorphous hill decreases with increasing ball-milling time, which can be attributed to (1) Fragmentation of Tm_2O_3 amorphization to few nanometer particles, because Tm_2O_3 is belong to a brittle component; (2) Dissolution of Tm and O atoms into Fe crystal structure to form a supersaturated nanocrystalline solid solution of Fe (Tm, O). Similar experiment phenomena were also observed in Huang's research [21] and Luo's report [9]. In the Mo-Tm_2O_3 system, the diffraction peaks of Tm_2O_3 phase disappeared after 24 h of ball milling and only Mo phase was observed after ball milling for 48 h [9]. In Pradyumna Kumar Parida's research, the diffraction peaks of Y_2O_3 phase disappeared and Fe component still could be observed after 30 h of ball milling [20].

Fig. 2 shows bright field TEM image, the corresponding selected area electron diffraction (SAED) pattern and energy dispersive spectrometer (EDS) results of Fe-Tm_2O_3 powder mixtures milled for 48 h. A dark particle is shown in Fig. 2(a). The SAED pattern taken from the region marked letter 'A' in Fig. 2(a) is shown in Fig. 2(b), which indicates a characteristic diffraction ring of nanocrystal materials. There are three diffraction rings including Fe (2 1 1), Fe (2 2 2) and Tm_2O_3 (4 4 4). A diffraction halo ring marked by two black circles in Fig. 2(b) can also be observed, which belongs to the amorphous Tm_2O_3. After ball milling for 48 h, Tm_2O_3 is partly amorphous, which is also proved by XRD pattern as shown in Fig. 1. Fig. 2(c) shows EDS results of the region marked the letter 'A' in Fig. 2(a), which includes the peaks of elemental Fe, Tm and O. Other particles also have similar EDS results.

Fig. 3 shows the relationship between the lattice constant and grain size of Fe phase and ball-milling time. It can be seen that there is a sharp decrease of Fe grain size in the initial stage and a slow one in the later stage with increasing ball-milling time. Finally, the grain size tends to a constant value, approximately 18 nm, after ball milling for 120 h. Owing to the crash between grinding balls and powder particles, the mixture powders are crashed, reunited and cold-welded, which lead the crystals to be fined obviously. With increasing ball-milling time, they became nano-crystallized gradually. Eventually, the grains tend to keep

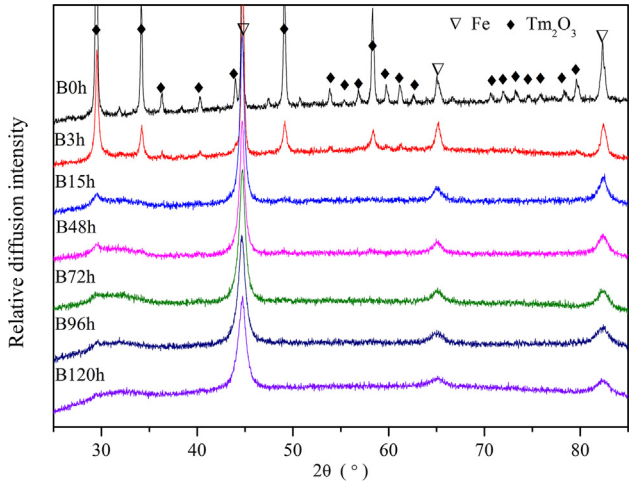

Fig. 1. XRD patterns of Fe-25.68 wt.%Tm_2O_3 powder mixtures milled for different time.

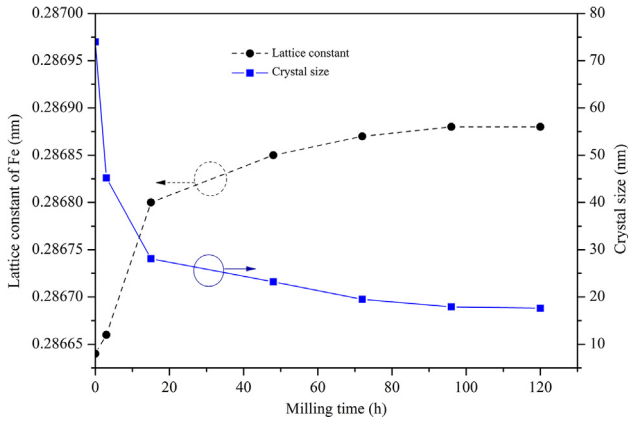

Fig. 3. The curves of lattice parameter and crystal size of Fe phase versus the ball-milling time.

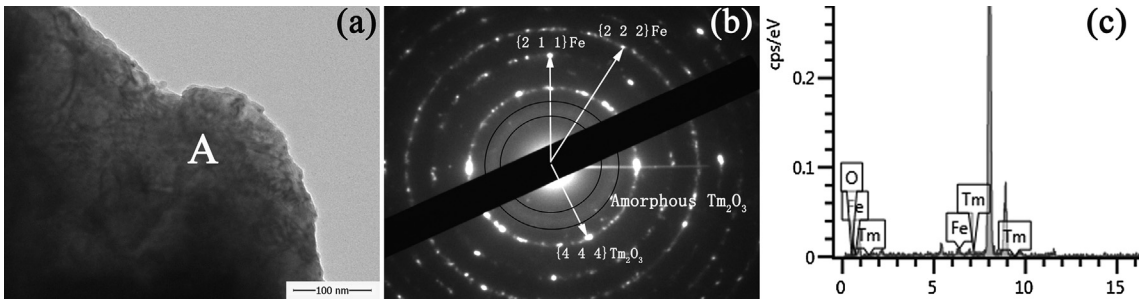

Fig. 2. Bright field TEM image (a), SAED pattern (b), EDS (c) of the Fe-Tm_2O_3 powder mixtures milled for 48 h.

constant. The variation tendency of the lattice constant of Fe phase is opposite. It increases fast at the early 15 h, changes slightly with the milling time adding, and keeps steady finally. Tm and O atoms dissolved into Fe crystal lattice is the main reason for the change of lattice constant.

3.2. Sintering behavior of the bulks

Fig. 4 shows the XRD patterns of the bulks prepared from Fe-25.68 wt.%Tm_2O_3 powder mixtures milled for 48 h and then sintered at different temperatures under #2 sintering condition. It can be seen that the XRD pattern of the bulk sintered at 600 °C is similar with that of the powder mixtures milled for 48 h. The obvious difference of XRD spectra between the sintered bulks and the ball-milled powders is only when the sintering temperature is over 700 °C. New diffraction peaks are observed in the XRD spectrum, which are proved as $TmFeO_3$ phase according to the JCPDS cards. It also indicates that there is a chemical reaction among Fe, Tm and O. At the sintering temperatures ranged from 700 °C to 1100 °C, the products have the same phase compositions, which means that the reactions happen at these temperature. Liu [12] used an *in-situ* high temperature XRD to find when the Fe-25% Y_2O_3 powders milled for 48 h was annealed at 800 °C, $YFeO_3$ was synthesized. TG-DAT results revealed that there was an exothermic peak between 700 °C and 800 °C that indicated an occurrence of chemical reaction.

The other transformation peak appeared at 1200 °C. It is interesting to note that $TmFeO_3$ phase disappears and Tm_2O_3 reappears after annealing at 1200 °C. According to the XRD results, it can be inferred that $TmFeO_3$ is decomposed to Tm_2O_3 and Fe between 1100 °C and 1200 °C.

Different sintering atmosphere will lead to different results. At the research system of the Fe-Y-O, Li [13] obtained the similar reaction phenomenon with us. However, the difference is that $YFeO_3$ was not found and only Fe and Y_2O_3 were detected when Fe-7.5%Y_2O_3 powders were annealed at hydrogen atmosphere. There was no a chemical reaction. According to the Li's report, the sintering atmosphere is very important. When the sintering conditions are changed, the experimental results will be also changed.

In the present work, in order to eliminate the effect of oxygen on the sintering results, the green bodies were also sintered at #1 experimental condition. The XRD patterns of the bulks sintered for different time at #1 experimental condition are shown in Fig. 5.

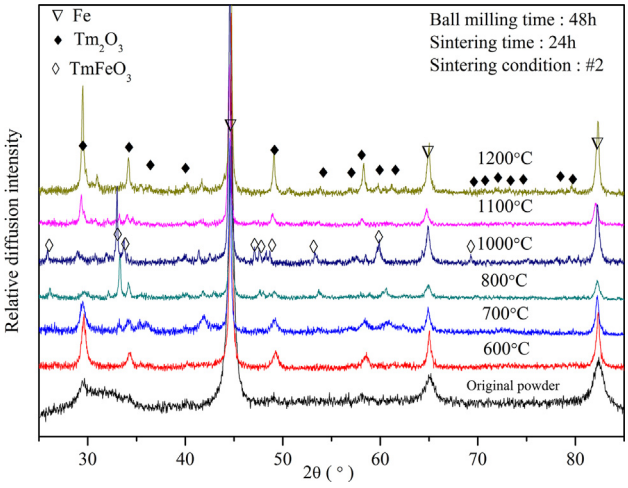

Fig. 4. XRD patterns of the bulks sintered for 24 h at different temperature under the #2 sintering condition.

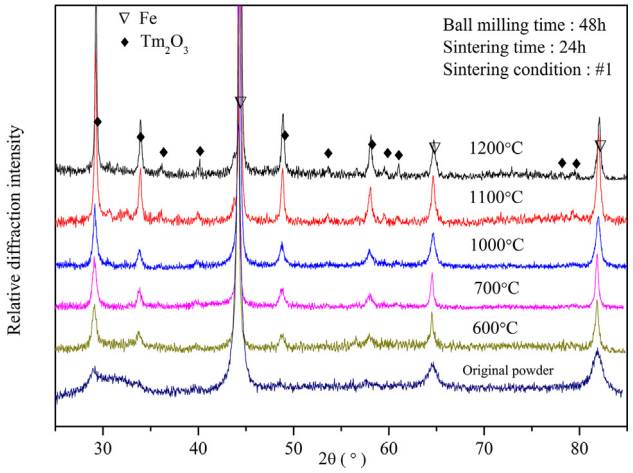

Fig. 5. XRD patterns of the bulks sintered for 24 h at different temperature under the #1 sintering condition.

At the temperature ranged from 600 °C to 1200 °C, only the diffraction peaks of Tm_2O_3 and Fe can be observed in the XRD spectra. $TmFeO_3$ phase was not found. It means that at #1 experimental condition there is not a chemical reaction between Fe and Tm_2O_3 at the sintering temperature ranged from 600 °C to 1200 °C.

To get $TmFeO_3$ phase, it may use Tm_2O_3 and Fe_2O_3 as initial reactant. The chemical reaction can be expressed as $Tm_2O_3 + Fe_2O_3 \rightarrow 2TmFeO_3$. Katsura [14] studied the thermodynamic properties of Fe-Tm-O compounds at high temperatures and obtained the phase change at 1200 °C. The oxygen pressure is a key factor that affects the chemical phase in the sintering system. Comparing the XRD results obtained at #1 and #2 experiment conditions, the biggest difference is whether the bulks were sealed in the crucible. Considering about the synthesis of $TmFeO_3$ phase reported in the references, it can be confirmed that the extremely low oxygen residual is the key reason affecting the reactions. Similar results were also found in the Fe-Y-O system [21], the oxygen partial pressures P_{O2} has a large influence on the final phases. When $-logP_{O2}$(atm) is 14.00, the phases are Fe and Y_2O_3. However, when $-logP_{O2}$(atm) is 13.28, the phases are Fe and $YFeO_3$.

Hsiung [22] studied Fe-20Cr-4.5Al-0.34Ti-0.5Y_2O_3 (designated as MA956) system and summarized the transformation progress of Al-Y_2O_3 to $Y_4Al_2O_9$ as three steps: (1) $Y_2O_3 \rightarrow 2[Y] + 3[O]$; (2) $2[Al] + [O] \rightarrow Al_2O_3$; (3) $2Y_2O_3 + Al_2O_3 \rightarrow Y_4Al_2O_9$. Consulting the Al-Y-O system, the transformation of Fe-Tm-O is similar. However, because of the residual oxygen in the crucible, the progress may have some differences. According to the equilibrium phase diagram of Fe-O system, when the oxygen pressure is extremely low, it easily forms FeO phase. The reaction process can be expressed as: (1) $O_2 \rightarrow 2[O]$; (2) $Fe + [O] \rightarrow FeO$; (3) $[Tm] + [O] \rightarrow Tm_2O_3$; (4) $2FeO + Tm_2O_3 + [O] \rightarrow 2TmFeO_3$. The transformation process can be concluded as:

$$Fe + 1/2\ Tm_2O_3 + 3/4\ O_2 \rightarrow TmFeO_3 \quad (1)$$

When the green bodies sealed without in the crucible are sintered at Ar atmosphere (#2 experiment condition), the reaction Eq. (1) will happen to form $FeTmO_3$ phase due to the residual oxygen in the ceramic tube. However, when the green bodies sealed within the crucible are sintered at Ar atmosphere (#1 experiment condition), there is almost no residual oxygen. The chemical reaction between Fe and Tm_2O_3 will not occur. These are also proved by the XRD diffraction patterns.

Fig. 6 shows the XRD patterns of the bulks sintered at different temperature for 24 h at the #2 experiment condition. It's aimed to

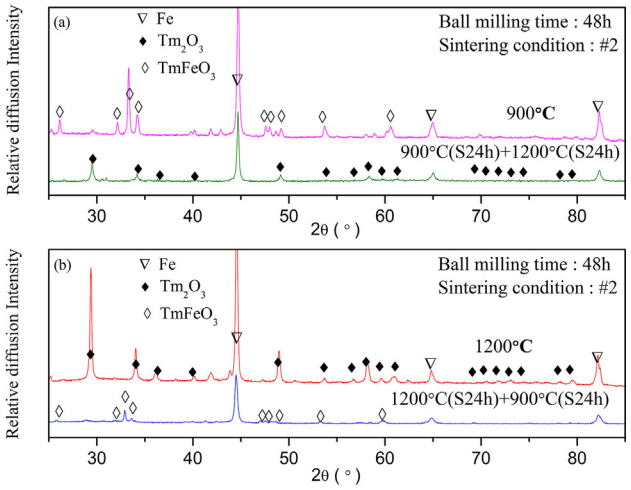

Fig. 6. XRD patterns of the bulks sintered at (a) 900 °C for 24 h and then at 1200 °C for 24 h; (b) 1200 °C for 24 h and then at 900 °C for 24 h at the #2 sintering condition.

study the transformation behavior between Tm_2O_3 and $TmFeO_3$. It can be seen that there are Fe and $TmFeO_3$ phase in the XRD spectrum after sintering for 24 h at 900 °C as shown in Fig. 6(a). However, the 900 °C-sintered bulks further sintered at 1200 °C for 24 h. The phases of sintered bulks change from the Fe and $TmFeO_3$ to the Fe and Tm_2O_3. Meanwhile, from the Fig. 6(b), there are also only Fe and Tm_2O_3 phases in the bulk sintered directly at 1200 °C for 24 h. However, when the 1200 °C-sintered bulks re-sintered at 900 °C for 24 h, $TmFeO_3$ phase occurs. Fe and Tm_2O_3 carry out a chemical reaction. Therefore, whether the transformation occurs or not, it's up to the temperature and the sintering atmosphere. In the service environment of nuclear reactor, the transformation among Fe, Tm_2O_3 and $TmFeO_3$ will not happen because the operation temperature (approximately 320 °C) is obviously lower than the above transition temperature.

Compared with Fe-Y-O system, the more interesting thing of Fe-Tm-O system is the mutual transformation between $TmFeO_3$ phase and Tm_2O_3 and Fe phases at specific sintering condition. According to Takashi Katsura's research [14], the equilibrium phase diagram of Fe-Fe_2O_3-Tm_2O_3 at 1200 °C shows that $TmFeO_{2.977}$ and Tm_2O_3 can coexist at an oxygen partial pressure of $10^{-10.25}$ atm. When the temperature rises to 1200 °C, the oxygen pressure is lower than that required and the reaction Eq. (1) will develop to the opposite direction, which leads to$TmFeO_3$ decomposition and Tm_2O_3 reappearance. The needless oxygen atoms will reunite with Fe atoms to form Fe_xO_y phase with the nonstoichiometry. However, the content is so low that it can't be detected by XRD method.

3.3. Microstructure of the sintered bulks

According to the above results, sintered at 1200 °C for 24 h, the 48 h-milled Fe-Tm_2O_3 powders will form Fe-based Tm_2O_3 composites at the #1 experiment condition and Fe-based $TmFeO_3$ composites at the #2 experiment condition. Bright field TEM images and EDS analysis results of the Fe-based Tm_2O_3 composite and Fe-based $FeTmO_3$ composite are shown in Fig. 7(a) and (b), respectively. Many particles with sizes ranged from dozens of nanometers to several hundred nanometers distribute in the Fe matrix as indicated by white arrows in Fig. 7(a). The EDS line-scanning results of the dark particle are inserted in Fig. 7(a). When the scanning line passes though the particle, the cps (contents per second) changes greatly. The atomic ratio of Tm to O meets 2:3 if the measurement error of EDS is considered. Therefore, the precipitates are Tm_2O_3 phase. Similar, for Fe-based $FeTmO_3$ composite, lots of particles also distribute in the Fe matrix as shown in the Fig. 7(b). The EDS analysis results show that the atomic ratio of Tm to O meets 1:3, which indicates the particle is $FeTmO_3$ phase.

3.4. Physical properties of the sintered bulks

Fig. 8 shows the curves of the thermal expansion of Fe-based Tm_2O_3 composites and Fe-based $TmFeO_3$ composites prepared by the Fe-Tm_2O_3 powder mixtures milled for different time. The sintering temperature and time are 1000 °C and 24 h, respectively. The coefficient of linear expansion increases with increasing ball-milling time and with increasing test temperature for these two kinds of composites. The increase of the coefficient of linear expansion is related to the different expansion coefficient of grain boundary and the grain. The expansion coefficient of grain boundary is larger than that of the grain. The long-time milling will lead the grain nanocrystallization and introduce a large amount of grain boundaries, which lead the increase of the coefficient of linear expansion. Meanwhile, under the same ball-milling conditions, the coefficient of linear expansion of Fe-based Tm_2O_3 composites is always smaller than that of Fe-based $TmFeO_3$ composites as shown in Fig. 8. In other words, Fe-based Tm_2O_3 composites have better thermal expansion resistance.

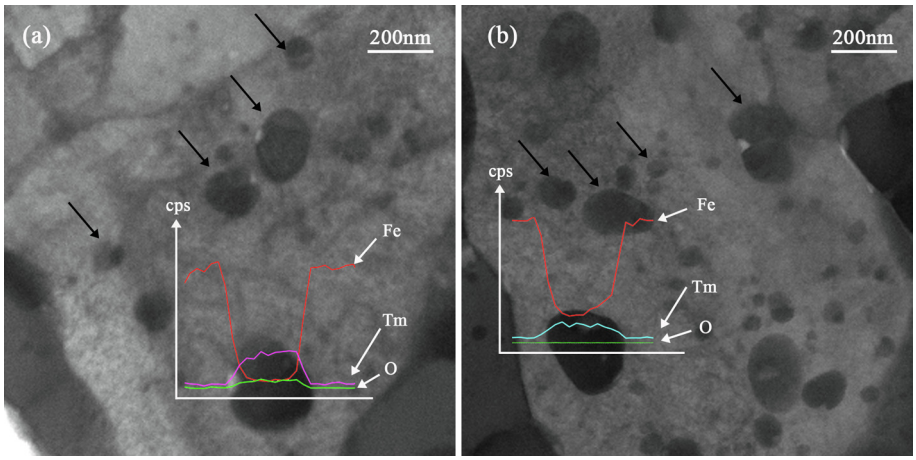

Fig. 7. TEM images and EDS results of (a) Fe-based Tm_2O_3 composites and (b) Fe-based $TmFeO_3$ composites.

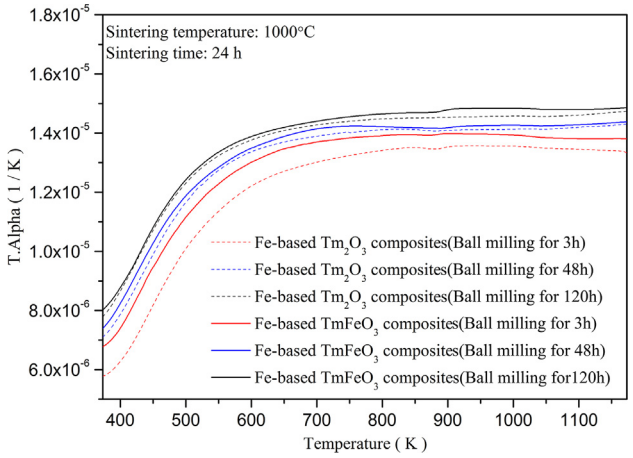

Fig. 8. The curves of the thermal expansion of Fe-based Tm_2O_3 composites and Fe-based $TmFeO_3$ composites. The sintering temperature and time are 1000 °C and 24 h, respectively.

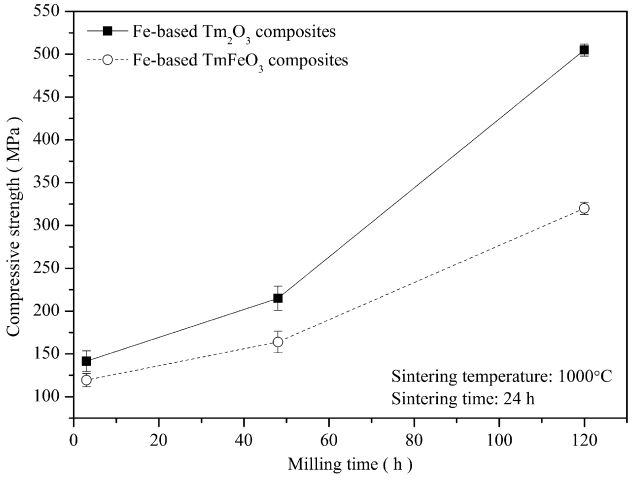

Fig. 10. Compressive strength of Fe-based Tm_2O_3 composites and Fe-based $TmFeO_3$ composite.

3.5. Mechanical properties of the sintered bulks

Fig. 9 shows the relationship between the average microhardness of Fe-based Tm_2O_3 composites and Fe-based $TmFeO_3$ composites and the sintering temperature. These sintered bulks were prepared by the Fe-Tm_2O_3 powder mixtures milled for 48 h. All bulks were sintered for 24 h. The microhardness was tested by a load of 100 g for 10 s on the sintered bulk surface at room temperature. The average microhardness comes from nine test values. It can be seen that the sintering temperature affects the microhardness. For both of Fe-based Tm_2O_3 composites and Fe-based $TmFeO_3$ composites, the microhardness increases with increasing sintering temperature when the test temperature is lower than 1200 °C in the present work. Meanwhile, the microhardness of Fe-based Tm_2O_3 composites is larger than that of Fe-based $TmFeO_3$ composites. The microhardness is up to the maximum value when the sintering temperature is at 1200 °C. At that temperature, the microhardness of Fe-based Tm_2O_3 composites and Fe-based $TmFeO_3$ composites are 123.6$HV_{0.1}$ and 119.1 $HV_{0.1}$, respectively. The biggest change rates of them come from the temperature between 1100 °C and 1200 °C, 0.45$HV_{0.1}$/°C and 0.380.45$HV_{0.1}$/°C respectively. The sintering temperature can improve the microhardness of these two materials at the temperature below 1200 °C.

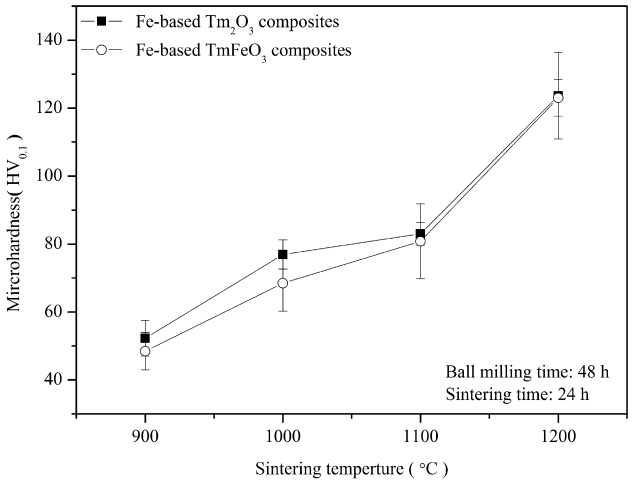

Fig. 9. Microhardness of Fe-based Tm_2O_3 composites and Fe-based $TmFeO_3$ composites.

Fig. 10 shows the relationship between the compressive strength and the ball-milling time. The ball-milling time has large influence on the compressive strength. The longer the ball-milling time of the mixture powders is, the larger the compressive strength of the bulks sintered at 1000 °C will be. Considering about the relationship between the gain size and the ball-milling time, the gain size of the ball-milled powders is a key factor to improve the compressive strength. In addition, from Fig. 10, the compressive strength of Fe-based Tm_2O_3 composites always larger than that of Fe-based $TmFeO_3$ at all experiment conditions.

4. Conclusions

The neutron absorbers of Fe-based Tm_2O_3 and Fe-based $TmFeO_3$ composites were synthesized by ball milling, cold isostatic pressing and sintering. The microstructure of the ball-milled powders and sintered bulks were investigated. The sintering behavior at different conditions was analyzed. The effect of preparation parameters on the microhardness, compression strength, and thermal expansion of the sintered bulks were also analyzed. The main conclusions could be made as followings:

(1) During the ball-milling process, Tm_2O_3 was fined, nanocrystallized and amorphized. After ball milling for 48 h, Tm_2O_3 phase completely transformed into the amporphization. Tm and O atoms dissolved into Fe crystal lattice to form Fe (Tm, O) nanocrystalline solid solution.

(2) The oxygen and temperature were the key factors affecting on the phase components of the sintered bulks. When the ball-milled Fe-Tm_2O_3 powders sintered in a sealed corundum crucible at argon atmosphere, Fe-based Tm_2O_3 composites were formed at the sintering temperature ranged from 700 °C to 1200 °C. However, without corundum crucible at argon atmosphere, Fe-based $TmFeO_3$ composites were acquired at the sintering temperature ranged from 700 °C to 1000 °C, which could be transformed to Fe-based Tm_2O_3 composites at 1100–1200 °C. Nanoscale $TmFeO_3$ and Tm_2O_3 particles were dispersive distributed in the Fe-based Tm_2O_3 composites and Fe-based Tm_2O_3 composites, respectively.

(3) Preparation parameters obviously influenced on the microhardness, compressive strength and coefficients of thermal expansion. The microhardness and compressive strength of Fe-based Tm_2O_3 composites were larger than that of Fe-based $TmFeO_3$ composites, opposite for the coefficients of

thermal expansion. The coefficient of linear expansion increased with increasing ball-milling time and with increasing test temperature. The microhardness increased with increasing sintering temperature when the temperature was lower than 1200 °C. The longer the ball-milling time of the mixture powders was, the larger the compressive strength of the bulks sintered at 1000 °C would be.

Declaration of Competing Interest

The authors declare no conflicts of interest.

Acknowledgements

The authors would like to acknowledge Mr. Yu Liu from Shanghai Jiaotong University for his support of thermal expansion experiment. The work was supported by National Natural Science Foundation of China, through Grant No. U1832112.

Author contributions

Guang Ran conceived and designed the experiments; Yongshuai Mu and Weisong Wu performed the experiments; Chao Ye and Yongshuai Mu obtained TEM results; Yongshuai Mu wrote the manuscript under the supervision of Guang Ran. All authors contributed to the scientific discussion of the results and reviewed the manuscript.

References

[1] H.W. Keller, J.M. Shallenberger, D.A. Hollein, A.C. Hott, Development of hafnium and comparison with other pressurized water reactor control rod materials, Nucl. Technol. 59 (1982) 476–482, https://doi.org/10.13182/NT82-A33005.
[2] D.R. Spink, J.H. Schemel, The development of rare-earth pyrohafnates for power reactor control-rod materia, J. Nucl. Mater. 49 (1973) 1–9.
[3] E.P. Klochkov, V.D. Risovanyi, Y.E. Vaneev, A.N. Dorofeev, Radiation characteristics of europium-containing control rods in a SM-2 reactor after long-term operation, At. Energy 93 (2002) 656–660, https://doi.org/10.1023/A:1021096715382.
[4] J. Huang, G. Ran, J. Lin, Q. Shen, P. Lei, X. Wang, N. Li, Microstructural Evolution of Dy_2O_3-TiO_2 powder mixtures during Ball Milling and Post-Milled Annealing, Materials (Basel) 10 (2017), https://doi.org/10.3390/ma10010019.
[5] Z.V. Eremeeva, V.S. Panov, L.V. Myakisheva, A.V. Lizunov, A.A. Nepapushev, D.A. Sidorenko, S. Vorotilo, Structure and properties of mechanochemically synthesized dysprosium titanate Dy_2TiO_5, J. Nucl. Mater. 495 (2017) 38–48, https://doi.org/10.1016/j.jnucmat.2017.07.058.
[6] V.D. Risovany, E.E. Varlashova, D.N. Suslov, Dysprosium titanate as an absorber material for control rods, J. Nucl. Mater. 281 (2000) 84–89, https://doi.org/10.1016/S0022-3115(00)00129-X.
[7] J. Lu, W. Yang, T. Liu, F. Zhang, G. Ran, L. Zhu, Preparation and properties investigation of neutron absorber material Fe-$TbFeO_3$-$DyFeO_3$, At. Energy Sci. Technol. 51 (09) (2017) 1716–1723, https://doi.org/10.7538/yzk.2017.51.09.1716.
[8] K. Wang, T. Liu, G. Ran, Y. Luo, J. Lu, N. Li, L. Wang, Investigation of Tb_4O_7-TiO_2 mixture powders prepared by high energy ball milling, RARE Met. Mater. Eng. 45 (09) (2016) 2462–2465, https://doi.org/10.1016/j.ijhydene.2015.05.098.
[9] Y. Luo, G. Ran, N. Chen, Q. Shen, Y. Zhang, Microstructural evolution thermodynamics and kinetics of Mo-Tm2O3 powder mixtures during ball milling, Materials (Basel) 9 (2016) 834, https://doi.org/10.3390/ma9100834.
[10] J.T. Yates, Spectroscopic studies of the thermal of the Fe/Al_2O_3 interface, Surf. Sci. 238 (1990) 13–24.
[11] K. Sakata, K. Ogawa, K. Nil, Interface chemistry and bonding strength for diffusion-bonded Fe/Fe-FeO/Al_2O_3 systems, J. Mater. Sci. 21 (1986), 0–4.
[12] T. Liu, H. Shen, C. Wang, W. Chou, Structure evolution of Y_2O_3 nanoparticle/Fe composite during mechanical milling and annealing, Prog. Nat. Sci. Mater. Int. 23 (2013) 434–439, https://doi.org/10.1016/j.pnsc.2013.06.009.
[13] W. Li, T. Hao, R. Gao, X. Wang, T. Zhang, Q. Fang, C. Liu, The effect of Zr, Ti addition on the particle size and microstructure evolution of yttria nanoparticle in ODS steel, Powder Technol. 319 (2017) 172–182, https://doi.org/10.1016/j.powtec.2017.06.041.
[14] T. Katsura, T. Sekine, K. Kitayama, T. Sugihara, N. Kimizuka, Thermodynamic properties of Fe-lathanoid-O compounds at high temperatures, J. Solid State Chem. 23 (1978) 43–57, https://doi.org/10.1016/0022-4596(78)90052-X.
[15] E.M. Baum, M.C. Ernesti, H.D. Knox, T.R. Miller, A.M. Watson, Nuclides and Isotopes:Chart of the Nuclides, Knolls Atomic Power Laboratory, 2009.
[16] J. Liu, W. Yang, L. Zhu, J. Lu, Q. Mei, C. Yao, L. Chen, W. Bi, An advanced gray control rods and absorber, CN102915772A, 2013.
[17] W. Yang, G. Bi, B. Yang, C. Tang, Study on production and validation of low worth control rod material burnup calculation parameters, Chinese J. Nucl. Sci. Eng. 48 (2014) 369–376.
[18] Y.V. Konobeev, A.M. Dvoriashin, S.I. Porollo, F.A. Garner, Swelling and microstructure of pure Fe and Fe-Cr alloys after neutron irradiation to ~26 dpa at 400 °C, J. Nucl. Mater. 355 (2006) 124–130, https://doi.org/10.1016/j.jnucmat.2006.04.011.
[19] N.I. Budylkin, E.G. Mironova, V.M. Chernov, V.A. Krasnoselov, S.I. Porollo, F.A. Garner, Neutron-induced swelling and embrittlement of pure iron and pure nickel irradiated in the BN-350 and BOR-60 fast reactors, J. Nucl. Mater. 375 (2008) 359–364, https://doi.org/10.1016/j.jnucmat.2008.01.015.
[20] P.K. Parida, A. Dasgupta, K. Jayasankar, M. Kamruddin, S. Saroja, Structural studies of Y2O3 dispersoids during mechanical milling and annealing in a Fe-15 Y_2O_3 model ODS alloy, J. Nucl. Mater. 441 (2013) 331–336, https://doi.org/10.1016/j.jnucmat.2013.06.016.
[21] K. Kitayama, M. Sakaguchi, Y. Takahara, H. Endo, H. Ueki, Phase equilibrium in the system Y-Fe-O at 1100°C, J. Solid State Chem. 177 (2004) 1933–1938, https://doi.org/10.1016/j.jssc.2003.12.040.
[22] L.L. Hsiung, M.J. Fluss, S.J. Tumey, B.W. Choi, Y. Serruys, F. Willaime, A. Kimura, Formation mechanism and the role of nanoparticles in Fe-Cr ODS steels developed for radiation tolerance, Phys. Rev. B - Condens. Matter Mater. Phys. 82 (2010) 1–13, https://doi.org/10.1103/PhysRevB.82.184103.